A test of the Hapke photometric model

Michael K. Shepard[1] and Paul Helfenstein[2]

Received 27 October 2005; revised 14 September 2006; accepted 21 September 2006; published 1 March 2007.

[1] We conducted a test of the Hapke (1981, 1984, 1986, 2002) photometric model to determine what physical parameters could be confidently linked to a surface's photometric behavior. The first author selected and measured the bidirectional reflectance distribution functions of 14 different samples in up to three different wavelengths using the Bloomsburg University Goniometer Laboratory. A total of 29 data files were obtained, each file containing more than 700 measurements from different viewing geometries; phase angles varied from 3° to 130°. The 29 files were initially sent "in-the-blind" to the second author, who was charged with inverting the data files and extracting best fit model parameters. Our baseline model used the most recent Hapke (2002) formulation with a two-term Henyey-Greenstein particle phase function and shadow-hiding backscatter opposition effect (SHOE) model. We also inverted the data with three other variations that included three-term Henyey-Greenstein phase functions and both SHOE and the coherent backscatter opposition effect (CBOE) models. Our results were compared with the known physical properties of our samples. We found no compelling evidence that individual photometric parameters could be uniquely interpreted to reveal the physical state of our samples, either in an absolute or relative sense. Rather, combinations of physical properties such as albedo, roughness, and porosity were convolved within each retrieved photometric parameter. On the basis of our empirical evidence, we speculate that the fault lies with the inability of radiative transfer models to adequately account for discrete media and the effects of porosity, and its deficient assumption that individual particles are the primary scattering units.

Citation: Shepard, M. K., and P. Helfenstein (2007), A test of the Hapke photometric model, *J. Geophys. Res.*, *112*, E03001, doi:10.1029/2005JE002625.

1. Introduction

[2] The Hapke photometric model [*Hapke*, 1981, 1984, 1986, 1993, 2002] (hereinafter referred to simply as the Hapke model) is the *de facto* standard for analyzing photometric data in the planetary and terrestrial remote sensing communities. Its derivation is based on first principles of radiative transfer and its primary applications have been to (1) correct imagery to standard lighting and viewing geometry for comparative or other purposes [e.g., *Simonelli et al.*, 1996; *Hudson and Ostro*, 1999]; (2) unmix spectra to estimate abundances and types of mixed materials [e.g., *Cruikshank et al.*, 2001; *Poulet et al.*, 2002]; and (3) estimate physical properties of a surface regolith including surface roughness, grain size, and porosity [e.g., *Mallama et al.*, 2002; *Buratti et al.*, 2004]. While the first two applications have been tested in the laboratory and practice, there have been few laboratory tests of the third application.

[3] The Hapke model is only one of several models that utilize radiative transfer methods to investigate the scattering properties of regoliths [e.g., *Lumme and Bowell*, 1981]. A fundamental assumption in the derivation of these models is that the surface medium is continuous, that is, nondiscrete. However, when used to interpret planetary photometry, it is commonly assumed that these models are also applicable to particulate surfaces in which the particles are in close contact [*Hapke*, 1993]. This assumption is often implicit and is so pervasive that the extracted parameters are usually assumed to be fundamental properties of the particles themselves. Recent work by a number of authors, but most notably *Piatek et al.* [2004], has brought this assumption into doubt. The major impetus for this work was to test the extent to which the Hapke parameters extracted from photometric data could be used to interpret the physical properties of the regolith. For example, does a larger roughness parameter correspond to a rougher surface? Does the average particle phase function allow us to distinguish between particles with moderate and low densities of internal scatterers? Given an estimate of the opposition surge width, can we deduce meaningful information regarding the surface porosity?

[4] For this work, the first author (MS) initially chose ten samples of different grain size, packing density, and composition. Four additional samples were selected and

[1]Department of Geography and Geosciences, Bloomsburg University, Bloomsburg, Pennsylvania, USA.
[2]Center for Radiophysics and Space Research, Cornell University, Ithaca, New York, USA.

0148-0227/07/2005JE002625

analyzed later and separately, bringing the total to fourteen samples. The bidirectional reflectance of each sample was measured by MS using the Bloomsburg University Goniometer Laboratory (BUG lab) at 770 different combinations of incidence, emission, and phase angle to characterize their bidirectional reflectance distribution function (BRDF). In several cases, samples with strong color contrasts were chosen and measured at multiple wavelengths to discern the effects of changing the average particle single-scattering albedo. Twenty-nine (29) complete sets of scattering data were chosen, given random file numbers, and sent to the second author (PH). He was not initially privy to the identity of any of the samples or even the wavelengths at which they were measured. PH was charged with inverting each data set to find the best Hapke model fits, and only later given a key to the samples so that he could contribute to the analysis. At one point after our initial fitting was complete, we discovered a software bug that required refitting all of our sample data. In all cases, PH fit data strictly by file number and not by sample identity to avoid biasing the outcome of the fits.

[5] In the following sections, we briefly describe the Hapke model, characteristics of the BUG lab, and our methodology in more detail. We then examine the results of the model fits, discuss the implications, and conclude with some suggested guidelines for interpreting model parameters.

2. Hapke Model Description

[6] For this work, we used the model for bidirectional reflectance in a semi-infinite particulate medium presented by *Hapke* [2002] with a two-term Henyey-Greenstein (2T-HG) average particle single-scattering phase function and a numerical calculation of multiple scattering that allows for anisotropic phase functions:

$$r(i,e,\alpha) = \frac{w}{4\pi}\frac{\mu_0}{\mu_0+\mu}[p(\alpha)B_{SH}(\alpha) + M(\mu_0,\mu)]B_{CB}(\alpha), \quad (1a)$$

where w is the single-scattering albedo, μ_0 and μ are, respectively the effective *cos*(i) and *cos*(e), each adjusted for the effects of average macroscopic roughness [*Hapke*, 1984], $p(\alpha)$ is the particle phase function (or more simply "phase function"), and M is Hapke's function [*Hapke*, 2002] to model the effects of multiple scattering from anisotropic scatterers. B_{SH} describes the shadow-hiding opposition effect (SHOE), and is defined by

$$B_{SH}(\alpha) = 1 + B_{0,SH}[1 + (1/h_{sh})\tan(\alpha/2)]^{-1}, \quad (1b)$$

where $B_{0,SH}$ is the amplitude ($\leq$1) and h_{sh} is the width. B_{CB} describes the coherent backscatter opposition effect (CBOE) and is defined by $B_{CB} = 1 + B_{0,CB}B_C(\alpha)$, where $B_{0,CB}$ is the amplitude ($\leq$1),

$$B_C(\alpha) = \frac{1+[(1-e^{-\gamma})/\gamma]}{2[1+\gamma]^2}, \gamma = (1/h_{cb})\tan(\alpha/2), \quad (1c)$$

and the width, $h_{cb} = \lambda/4\ \pi\Lambda$, where λ is the wavelength and Λ is the transport mean free path in the medium. All of these are parameters are discussed in more depth by *Hapke* [2002]. We also included Hapke's surface roughness correction and associated parameter $\overline{\theta}$ (theta bar) in accordance with the equations outlined by *Hapke* [1984, 1993].

[7] We initially assumed that all of the opposition effect was due to shadow hiding (SHOE) and ignored coherent backscattering (CBOE) as a contributor; this decision was based on the lowest phase angle measured (3°) and the observation that coherent backscattering is usually (although not always) dominant at phase angles less than this [e.g., *Helfenstein et al.*, 1997; *Shkuratov et al.*, 1997; *Hapke et al.*, 1998; *Nelson et al.*, 2000].

[8] Subsequent to our initial analysis, we went back and refit all the data using the same model but included the CBOE, and the same model with a three-term HG function (3T-HG), with and without the CBOE mechanism [*Hapke*, 2002]. In all, we ended up with four separate model fits per sample. Although the second author was aware of the sample identities when conducting the latter three fits, these were performed as a batch by file number and not by sample identity to prevent biasing the outcomes. We conducted these latter model fits to test the robustness of various model parameters and to look for correlations and trade-offs in the various model parameters [e.g., *Helfenstein and Veverka*, 1989; *Hartman and Domingue*, 1998].

2.1. Single-Scattering Albedo (w)

[9] The average particle single-scattering albedo, w, is defined as the ratio of the amount of light at a given wavelength scattered from a representative incremental volume of a medium to the combined amount of light scattered from and absorbed by it:

$$w = \frac{S}{S+K}, \quad (2)$$

where S is the scattering coefficient, the fraction of light scattered from the medium, and K is the absorption coefficient, the fraction of light absorbed by the medium. The admissible range of values for single-scattering albedo is thus $0 \leq w \leq 1$. In most applications, it is assumed to be an average property of the particles making up the medium and therefore to depend on the optical constants of the particle, its size, and to some extent its shape and internal structure [*Hapke*, 1981; *Hapke and Wells*, 1981]. Particles composed of nonabsorbing materials generally have large values of w. For soil particles, where grains are in mutual contact and it is assumed that particles are generally much larger than a wavelength of light, as particle size decreases, w increases for all but the most absorbing materials. Large particles and particles with moderate to high imaginary indices of refraction tend to absorb a larger fraction of the incident light and therefore tend to smaller w.

[10] Although often interpreted as an isolated property of a medium, the single-scattering albedo is actually an integral component of the particle phase function. [cf. *Chandrasekhar*, 1960]. Particles with lower single-scattering albedos tend to be more opaque than higher-albedo grains and consequently, we might expect the corresponding particle phase functions to be more strongly backscattering. The single-scattering albedo is also coupled to other scattering phenomena in the regolith. For example, the ampli-

tude of SHOE is affected by particle transparency; larger amplitudes are expected for more opaque particles since they cast darker shadows. Finally, in theory, the angular width of CBOE is expected to be wider in regoliths composed of dark scatterers than for those made of more transparent grains.

2.2. Surface Roughness ($\bar{\theta}$)

[11] Hapke's roughness correction factor, $\bar{\theta}$, is one of the more widely interpreted parameters and has traditionally been thought to be related to the integral surface roughness at sensor subpixel scales [*Hapke*, 1984; *Helfenstein*, 1988]. However, it has been suggested by several authors that the microscale surface roughness is the most relevant scale [*Akimov*, 1988; *Shkuratov and Stankevich*, 1997; *Shepard and Campbell*, 1998; *Helfenstein and Shepard*, 1999].

[12] Unfortunately, both the opposition surge and particle phase functions can mimic the phase angle effects of macroscopic surface roughness at small phase angles. Disk-resolved coverage from limb to terminator and observations at large phase angles are thought to be necessary for constraining surface roughness [*Helfenstein*, 1988; *Helfenstein and Veverka*, 1989].

2.3. Opposition Surge (h and B_0)

[13] The opposition surge is the nonlinear increase in brightness with decreasing phase angle observed near $\alpha = 0$. Its origin and interpretation are still debated. Although originally interpreted by *Seeliger* [1895] as due to shadow hiding, the most recent interpretations of the effect include coherent backscattering as a greater or lesser contributor [cf. *Hapke et al.*, 1998; *Helfenstein et al.*, 1997; *Muinonen*, 1990; *Mishchenko*, 1992; *Shkuratov et al.*, 1994; *Nelson et al.*, 2000]. As noted above, we initially chose to assume that the entire opposition surge is due to the shadow-hiding opposition effect (SHOE) based primarily upon the phase angle limitations of the BUG lab ($\alpha \geq 3°$) and the phase angles at which the coherent backscatter opposition effect (CBOE) appears to dominate ($\alpha < 2°$) in experimental observations. In addition, the two effects are difficult to separate without circular polarization data [*Hapke*, 2002]. However, to examine how the SHOE and CBOE components interact, our latter fits included the CBOE contribution.

[14] *Hapke* [1986, 1993] defines the amplitude of the shadow-hiding opposition surge as

$$B_{0,\mathrm{SH}} \cong \frac{S(0)}{wP(0)}\ , \tag{3}$$

where $S(0)$ is the amount of light scattered at or close to the particle surface (e.g., Fresnel reflectance) and $P(0)$ is the value of the particle phase function evaluated at zero phase so that the quantity $wP(0)$ represents the *total* amount of backscattered light from a particle at zero phase. Physically, a value of $B_{0,\mathrm{SH}} = 1$ suggests the presence of opaque particles or aggregates of particles in which first surface reflections are dominant. Transparent particles high in albedo (w) and particles for which most of the backscattered light is scattered from the particle interior (large $P(0)$) increase the denominator; $B_{0,\mathrm{SH}} < 1$ therefore suggests grains of either increasing transparency or alternatively, increasing volume scattering from scatterers within grains composed of nonabsorbing materials.

2.4. Phase Function (b and c, or g_1, g_2, and f)

[15] Nearly all phase functions in use are empirical and based on easily quantified and normalized functions. The most commonly used phase functions are Legendre polynomials of one or two terms [cf. *Hapke*, 1981] and Henyey-Greenstein (HG) functions of 1, 2, or 3 terms [cf. *McGuire and Hapke*, 1995; *Hartman and Domingue*, 1998]. On the basis of a survey of recent literature, the HG is the more preferred, and this is the form that we chose to use.

[16] The two-term HG function (2T-HG), defined as

$$p(\alpha) = \frac{1+c}{2}\frac{1-b^2}{(1+2b\cos\alpha+b^2)^{1.5}} + \frac{1-c}{2}\frac{1-b^2}{(1-2b\cos\alpha+b^2)^{1.5}}, \tag{4}$$

constrains the forward and backscattering lobe of a particle to be of the same angular width (b), but partitions their relative magnitude (c). A negative value of c indicates a particle is more forward scattering ($-1 < c < 0$), while a positive value indicates backscattering ($1 > c > 0$); $c = 0$ indicates the scattering is isotropic.

[17] The three-term HG (3T-HG) function is defined as

$$p(\alpha) = (1-f)\frac{1-g_1^2}{\left(1+2g_1\cos\alpha+g_1^2\right)^{1.5}} + f\frac{1-g_2^2}{\left(1+2g_2\cos\alpha+g_2^2\right)^{1.5}}, \tag{5}$$

where f is the partition coefficient, and g_1 and g_2 describe the relative widths of the two independent scattering lobes. Parameters of the 2T-HG function can be converted into those of the 3T-HG function as $g_1 = -g_2 = b$ and $f = (1 - c)/2$.

[18] *Hartman and Domingue* [1998] considered the relative merits of both functions and concluded that there was no improvement in the fit obtained by using the 3T-HG over the 2T-HG function when phase angles were limited to <130°. This mirrors our own findings. We also found the 3T-HG function to be more difficult to work with at this range of phase angles, apparently because it introduced too many free parameters and gave many identical, but parametrically ambiguous fits.

3. BUG Lab Specifications

[19] The BUG lab consists of three independent devices: (1) a CCD video camera with macrozoom lens and video capture system; (2) a single-grating VISIR spectrometer (LineSpec) sensitive from 0.4–0.9 um, and (3) a fully automated goniometer.

3.1. Video Camera System

[20] The purpose of this system is to photographically document the samples measured by the goniometer. It consists of a Panasonic GP-KR22 digital color video camera and 10x macrozoom lens. Images are captured with a Bandit™ video capture board. The image size is

480 × 640 pixels. The camera and lens are mounted such that the highest magnification gives a horizontal field of view (FOV) of 1 cm, resulting in a resolution of 12.5 μm/pixel. Tests with calibrated resolution charts show the highest useful resolution to be ~70 μm (~15 lp/mm).

3.2. Spectrometer

[21] The purpose of this system is to spectrally characterize and document the samples measured by the goniometer. It consists of a MS127 Spectrograph with LineSpec CCD detector head, and fiber-optic reflectance head attachment, all from Oriel Instruments. The reflectance head attachment measures the biconical reflectance of the sample using a quartz halogen bulb source and fiber optic light guide connected to the detector. The incidence angle is $i \sim 15°$, emission angle is $e \sim 10°$, and azimuth angle is $a \sim 200°$ (just out of the principal plane). The overall phase angle is $\alpha \sim 25°$. Although the detector is rated for 0.2–1.0 μm, the quantum efficiency of the detector and transmittance characteristics of the fiber optic cable effectively limit the useful range to 0.4–0.9 μm. The detector was calibrated using gas emission lines from H and Hg vapor lights. Spectral resolution is ~10 nm. We have empirically compared the spectra of identical samples taken with our instrument and a more sophisticated hemispherical reflectance spectrometer at JSC (R. Morris, personal communication, 2003) and found them to agree in shape and reflectance within ±20%.

3.3. Goniometer

[22] The goniometer consists of a quartz halogen source and solid-state detector moved along three independent axes by stepper motors. The source is a 100 W quartz halogen bulb which is (1) filtered to the desired wavelength using interference filters, (2) chopped, (3) focused onto a fiber optic bundle, and (4) routed to the end of a 0.6 m source arm where it is collimated and directed onto the sample. An electronic feedback system maintains light output constant to within ~1%.

[23] The source arm moves 0–65° in incidence (i) and 0–180° in azimuth (a). Our limitations in incidence angle (i) are based on sample size restrictions. A sample dish is 5.6 cm in diameter and the source beam creates a spot ~2 cm in diameter at nadir. As incidence angle increases, the spot elongates into an ellipse of major axis 2/cos i. At 65°, the ellipse major axis is ~5 cm. Samples larger than 6 cm in diameter will not fit within the confines of the sample space. Given the spot size and distance of the source from the sample, measurements at a reported incidence angle are due to a convolution of rays that impinge upon the surface at $i \pm 1°$.

[24] The solid-state detector is at the end of a 0.8 m arm and moves 0–80° in emission angle (e). It is electronically connected to the chopper on the light source to maximize signal-to-noise. Because the optics of the source occult the detector, phase angles (g) are limited to $g \geq 3°$. The detector sees the entire sample, even the nonilluminated portions, so that the observed intensity of incident light is a constant. Given the detector's diameter (1 cm) and distance from the sample, our measurements at a reported emission angle are due to a convolution of rays reflected from the surface at $e \pm 0.4°$.

[25] All three stepper motor stages and the detector are controlled with a PC and LabView™ software. Our stepper motor stages have a precision and repeatability of 0.001°. Absolute accuracy of pointing is ≤0.5°. Relative accuracy of pointing (with respect to the other arm) is ≤0.25°.

[26] The detector measures raw intensity in voltage. In order to derive reflectance values, we calibrate each run by measuring the voltage obtained from a spectrahalon reference (certified with respect to NIST standards) measured at $i = 0°$ and $e = 5°$.

[27] The desired positions of the various arms are sequentially scripted into a movement file. The software moves the arms to the first script position, waits 3–5 s for movement to dampen, records the intensity, and moves to the next position, etc.

[28] We estimate the relative uncertainties in our measurements by making duplicate measurements in the same geometries at different times within a given run. In most cases, differences are <1%. At extreme geometries ($i = 60°$, $e = 80°$) differences can be as high as 10%–15%. Some of this appears to be a signal-to-noise issue: at these extreme angles the detectable voltage is ~15% of its nadir value for a Lambertian sample. However, we also found evidence for a small systematic error (≤0.02 radiance factor units) that we later attributed to secondary reflections at the highest phase angles (~135°–140°) in and around the principle scattering plane. To avoid this, we limited our analysis to phase angles ≤130°. Overall, reflectance measurements are repeatable with an RMS dispersion of <5%. Our estimate of standard errors for absolute reflectance is ±15%. For estimating goodness of fit, we applied the following rule for the uncertainty in any given measurement: our measurement uncertainty is the larger of 10% of the radiance factor or 0.01 radiance factor units. This is because the uncertainties in the darker samples are noise limited.

4. Methodology

[29] For our test we chose a very diverse suite of samples on the basis of their availability, grain size, shape, and color contrast in the visible, but we made no attempt to select samples that are mechanical or compositional analogs to planetary regolith materials. Nevertheless, we believe our results have direct import to observations of planetary surfaces. Although regolith covered surfaces on many airless bodies may constitute a special category of photometric targets because of their structural complexity, the Hapke model was originally derived for aggregates of equant particles such as those we have tested. We expected that, at size scales relevant to photometric analysis, the main differences in photometric behavior would be due to composition, mean grain size, and perhaps packing density. We believed the strongest effects were likely to be caused by differences in composition, which are manifested as differences in optical constants of constituent materials that lead to differences in particle albedo. Our tests of strongly colored materials were designed to test this. In two instances, we measured the same sample in loose and compressed states to observe differences in packing density. We measured one sample in four different grain sizes to observe the affect of grain size. All samples chosen had uniform or near-uniform grain size distributions to minimize complications

Table 1. Sample Properties[a]

Sample	Abbreviation	D, μm	p,%	Notes
Aluminum oxide	AO120	106 ± 60	58	commercial-grade abrasive
Aluminum oxide	AO220	51 ± 22	59	commercial-grade abrasive
Aluminum oxide	AO320	26 ± 10	61	commercial-grade abrasive
Aluminum oxide	AO500	12 ± 4	71	commercial-grade abrasive
Blackbird clay	BCl	$\leq$1	84	loose, ~10–50 μm aggregates
Blackbird clay	BCp	$\leq$1	67	packed sample
Cobalt carbonate	CC	12 ± 5	93	small, spherical grains
Cobalt oxide	CO	19 ± 12	83	very dark, dense powder
Chromium oxide	CRl	$\leq$1	84	loose sample
Chromium oxide	CRp	$\leq$1	71	packed sample
Red iron oxide	FE	4 ± 3	84	~100 μm aggregates
Kualua sand	KS	530 ± 200	47	mixture of multicolored grains
Manganese oxide	MO	125 ± 56	67	very dark powder
Ooitic sand	OS	310 ± 95	45	pearly, rounded aragonite grains
Quartz sand	QS	310 ± 80	50	translucent, equant grains
Spodumene	SP	70 ± 40	60	translucent, lathe-like grains

[a]List of samples measured, sample abbreviation, mean grain size (in micrometers), bulk porosity, p (in percent), and notes for each. Uncertainties in grain size are one standard deviation and based either on accompanying literature (AO samples) or visual estimates from optical and electron microscopy. Bulk porosity was estimated for each by weighing sample to nearest 0.01 g, and using known sample volume and grain density from the literature. Uncertainties in porosity are estimated to be ±15% of the listed value.

in our physical interpretations. Table 1 lists the sample name, grain size, and porosity.

[30] In all cases, the surface was made as smooth as physically possible by carefully scraping it even with the sample dish and then gently tapping to settle the contents evenly and randomize the surface morphology. Each sample was then weighed to a precision of 0.01 g. Given the known volume of the sample dish and the weight, we calculated bulk porosity. Each sample was photographed with the video system at two scales: a low-resolution scale (~6 cm FOV, 0.1 mm/pixel) and high resolution (~1 cm FOV, ~15 μm/pixel). Grain sizes were determined by

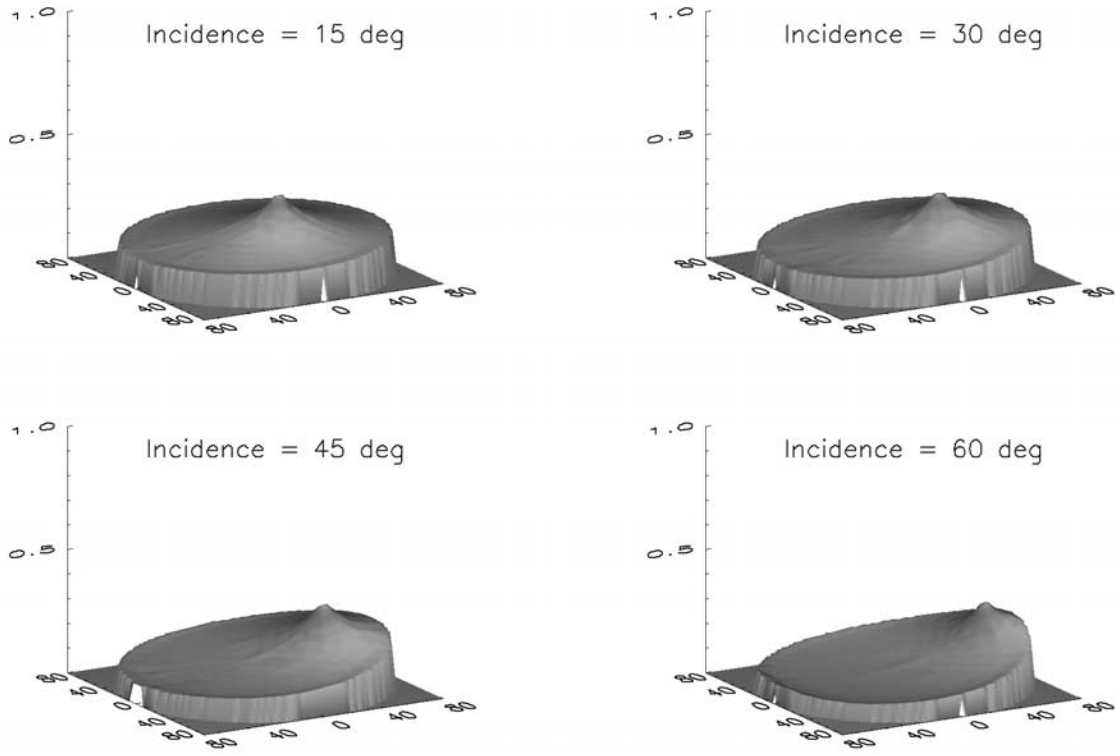

Figure 1. Example of the scattering data acquired by the goniometer during a typical run. The data shown here are for sample FE at 700 nm. Each plot shows data acquired at a single incidence angle as labeled. The z axis is radiance factor (ratio of measured detector voltage from the sample to that of a spectralon reference measured at $i = 0°$, $e = 5°$). Emission angle is radial from the center of the plot, 0° at center, 80° at perimeter. Azimuth angle is clockwise from far right. Note the opposition surge and strong backscattering behavior. A Lambertian surface would have a constant value, flat surface plot.

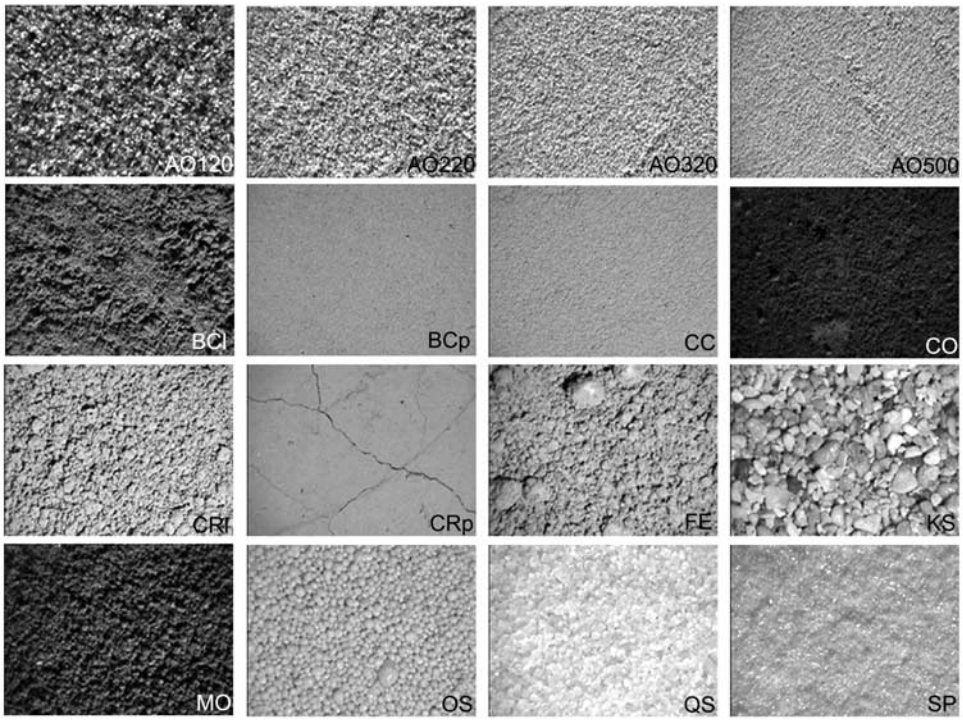

Figure 2. Mosaic of high-resolution optical images of samples investigated. Field of view for each image is 1 cm.

sample documentation or inspection and measurement from the digital images or electron micrographs acquired later.

[31] Each sample was measured at the same combination of incidence, emission, and azimuth angles. Incidence angle was varied in five steps; 0°, 15°, 30°, 45°, and 60°. For each step in incidence, emission angle was varied from 0° to 80° in increments of 10°. For all incidence angles except 0°, azimuth was varied from 0° to 180° in steps that varied with emission angle. The goal was to measure the majority of the BRDF in ~0.05 steradian increments. For each incidence angle, a total of ~150 different emission and azimuth angles were measured. At 10° on either side of opposition, emission angles were incremented 1° to our limiting minimum phase angle of 3°. This measurement density was also used near the specular point. Figure 1 shows an example of the type of data obtained for each sample at a given wavelength.

4.1. Fitting Algorithm

[32] The computer program used to obtain least squares fits of Hapke's model to the laboratory reflectance data is described in detail by *Helfenstein* [1985]. This algorithm for finding optimal values of Hapke parameters is a hybrid method that incorporates simultaneous stepwise grid searching of parameter space and gradient following to locate the minimum weighted mean-square residual, χ^2 between the measured and modeled values of radiance factors,

$$\chi^2 = \sum_j \left[\frac{r_j - r_{model}(i_j, e_j, \alpha_j)}{\sigma_j} \right]^2, \qquad (6)$$

where r_j is the measured radiance factor of data point j, σ_j is the corresponding measurement uncertainty, i_j, e_j, α_j are the corresponding values of incidence angle, emission angle, and phase angle, respectively, and $r_{model}(i_j, e_j, \alpha_j)$ is the Hapke-predicted value of the radiance factor.

4.2. Uncertainties

[33] We computed formal error bars for each fit. The standard criterion used was that the uncertainty in any given parameter was the amount of parameter value change that worsened the RMS residual by the average uncertainty in measured absolute reflectances (i.e., 15%). The estimate took into account parameter coupling: that is, other Hapke parameters can change to compensate for changes in the tested parameter. However, this resulted in average parameter uncertainties which seemed unrealistically large, especially given that we had supplied a wide range of photometric geometries. This probably results from the fact that Hapke's model relies on parameters that are not truly independent and may render this standard error estimation approach meaningless.

[34] As an alternate approach, we examined the parameter dispersion that resulted from fitting the variants of the Hapke model described in section 2. Using this approach, we find average uncertainties in our nominal parameter fits that are more in-line with our expectations and values typically reported in the literature. In addition, we believe this to be more realistic because we are assessing how much uncertainty is due to the form of the particle phase function used and whether CBOE is included or not.

[35] An ideal data set would cover phase angles from 0° to 180°. However, complete data sets such as these are rare in the laboratory and nearly absent in planetary observations. Our data set, while limited in phase angles from 3° to 130°, is more extensive in coverage than the majority

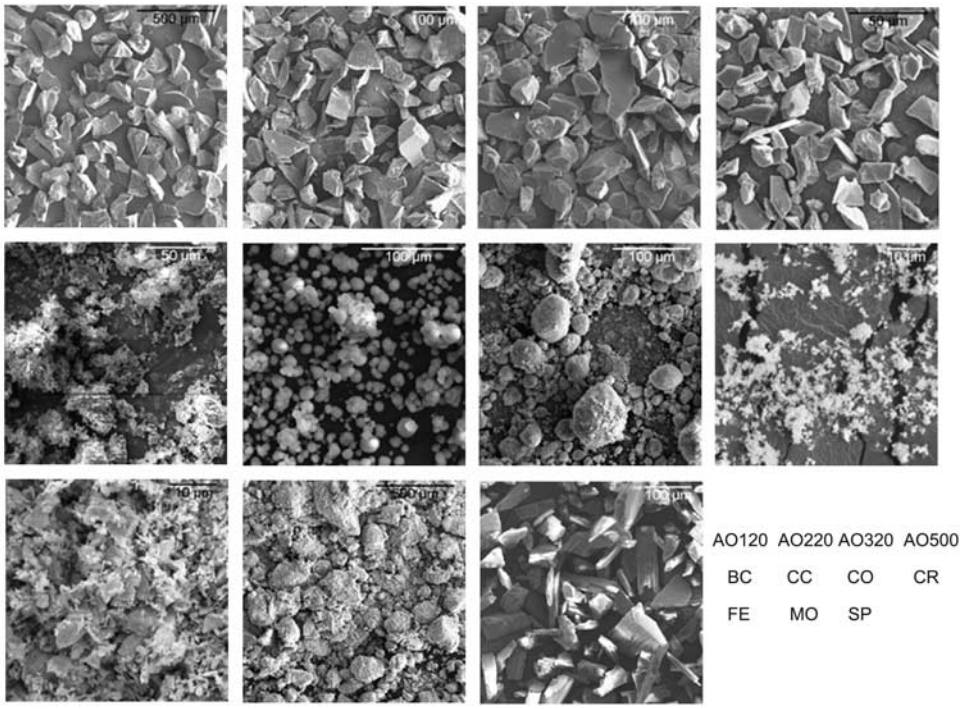

Figure 3. Mosaic of scanning electron microscope (SEM) images of most samples investigated. Field of view for each image is in the upper right corner. No images were acquired for Kualua sand (KS), ooitic sand (OS), and quartz sand (QS), because these were large enough to inspect with the optical images (Figure 2). The aluminum oxide (AO) samples were imaged to ensure that particle size distributions were as expected and that the methods we used to estimate particle sizes for other samples were accurate.

of planetary data sets and provides a real test of what can and cannot be extracted with confidence from them.

5. Sample Descriptions

[36] Table 1 lists the physical properties of each sample. The following figures document their physical characteristics and scattering behavior: Figure 2 shows a mosaic of sample images at our highest magnification (FOV $\sim$ 1 cm); Figure 3 shows representative scanning electron microscope (SEM) images; Figure 4 shows our spectrum of each sample; and Figure 5 shows plots of radiance factor (RF) versus emission angle for $i = 0^\circ$ with best fit model superposed.

[37] With the exception of the aluminum oxide samples, we will refer to the sample and the wavelength at which it was measured as XX-550, where the XX is a sample abbreviation (given below), and the 550 indicates it was measured at 550 nm. The aluminum oxide samples were all measured at the same wavelength (700 nm), so the number after each refers to the sample mesh size rather than measurement wavelength (e.g., AO120 is the 120 mesh sample).

[38] Particle sizes for each sample were measured using the optical or SEM images as appropriate. The commercially sieved aluminum oxide samples served as a reliability control for this method. All of our samples have relatively narrow size distributions and the one standard deviation width of the distribution is listed as an indication of the size dispersion.

5.1. Aluminum Oxide (AO)

[39] Four different mesh sizes of a commercial-grade aluminum oxide abrasive (Willman-Bell) were obtained; 120, 220, 320, and 500 sieve (125 μm, 63 μm, 45 μm, and 25 μm, respectively). Estimates of grain size using scanning electron micrographs show the average to be consistent with average particle sizes reported for abrasives of these mesh sizes (Table 1). The primary purpose of measuring these samples was to examine the effects of grain size while controlling composition. All of the samples are spectrally flat. We measured all of these at 700 nm wavelength, and refer to them in the text as AO120, AO220, etc.

5.2. Clay (BCl and BCp)

[40] Sold under the name ''blackbird clay'' as a glaze for potters, this is an illite-dominated clay with significant hematite abundance. Individual grains are difficult to discern even with electron microscopy but appear to be micron-scale. The dominant structure appears to be particle aggregates 10–50 μm in scale. It is spectrally red. Samples were acquired for both loose (*BCl*) and packed states (*BCp*) to observe the affects of porosity on the same sample. This sample was also measured in three wavelengths to observe the affects of changing albedo.

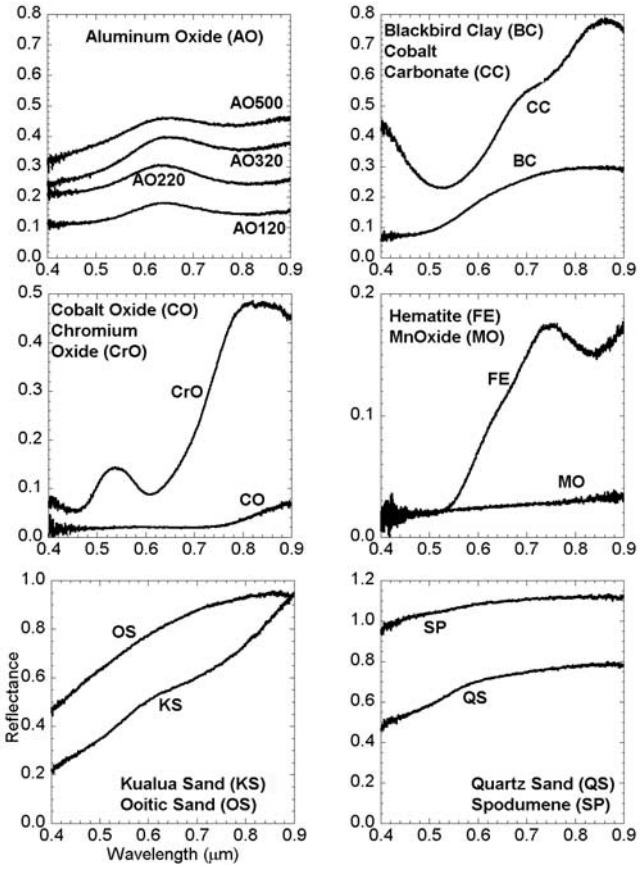

Figure 4. Mosaic of sample spectra acquired with the LineSpec spectrometer. The y axis is reflectance relative to a spectralon reference. The x axis is wavelength, 0.4–0.9 μm. Individual graphs are labeled with sample abbreviations.

5.3. Cobalt Carbonate (CC)

[41] This sample has one of the smaller grain sizes in our sample ($\sim$12 μm). Grains are uniform in size and rounded in shape. Spectrally, it shows an absorption in the green and was measured in three wavelengths to observe the effects of changing albedo.

5.4. Cobalt Oxide (CO)

[42] This is a dark and dense powder. Grains are small ($\sim$20 μm) but spheroidal. It is spectrally dark and flat and most useful to compare with MO.

5.5. Chromium Oxide (CRl and CRp)

[43] The particles of this sample (Cr_2O_3) are extremely fine ($\leq$1 μm) and tend to clump into larger aggregates of up to 1 mm in diameter. Our sample was an intense green color and has a spectral peak at 530 nm in the visible spectrum. Samples were acquired for both loose (*CRl*) and packed states (*CRp*) to observe the affects of porosity on the same sample. This sample (each packing state) was measured in two wavelengths to observe the affects of changing albedo.

5.6. Red Iron Oxide (FE)

[44] X-ray diffraction shows this to be primarily hematite (Fe_2O_3). Grains are complex in shape and approximately 4–10 μm in size; as with BCl, it tends to form larger scale ($\sim$100 μm) structures. It is spectrally red and was measured in three wavelengths to observe the effects of changing the albedo without modifying the particulate or surface structure.

5.7. Kualua Sand (KS)

[45] A sample of sand from Kualua beach, Hawaii, was obtained from a colleague. The grain size is nearly uniform at $\sim$500 μm, yet the sample is a micromixture of different opaque grains. It is most useful to compare with ooitic sand and quartz sand (below), both of which have nearly identical grain sizes, but dramatically different particle proper-

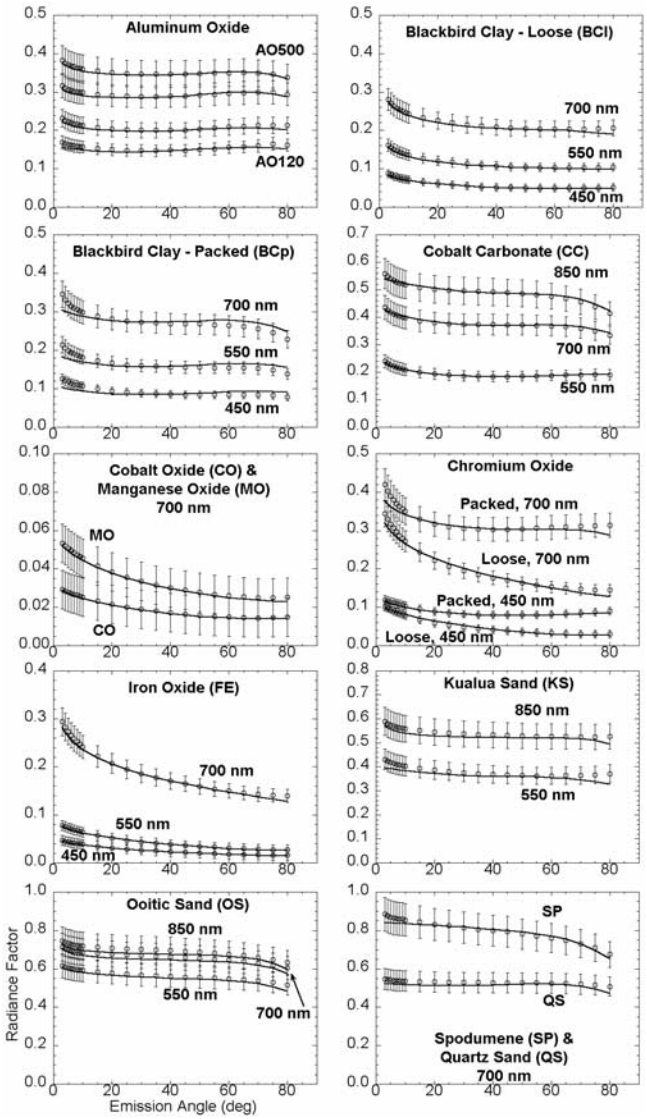

Figure 5. Mosaic of sample scattering behavior for $i = 0$. Y axis is radiance factor, and x axis is phase angle. Individual graphs are labeled with sample abbreviations. Error bars indicate those used in the model fit (see text). The solid lines are the best two-term Henyey-Greenstein (2T-HG) with shadow-hiding opposition effect (SHOE)-only model fits.

ties. This sample shows a strong spectral reddening and was measured in two wavelengths.

5.8. Manganese Dioxide (MO)

[46] This is a dark powder with equant grains an order of magnitude larger than CO. The grains, while equant, are exceedingly rough at the ~5 μm scale. High-magnification electron micrographs suggest our "particles" may be composites of much smaller particles. It is spectrally flat.

5.9. Ooitic Sand (OS)

[47] This is a sample of nearly pure aragonitic ooids. Grain size is uniform at ~300 μm, and the shape is nearly spherical. It is best compared with Kualua sand and quartz sand. Grain appearance would best be described as pearly. It is spectrally red and was measured in three wavelengths.

5.10. Quartz Sand (QS)

[48] This is a sample of nearly pure quartz sand. Grain size is uniform at ~300 μm and the shapes are equant. Grains are nearly transparent. It is best compared with Kualua sand, ooitic sand, and spodumene (below). Spectrally, it is slightly reddened.

5.11. Spodumene (SP)

[49] This is a sample of crystalline spodumene. Grain size is ~70 μm, grains are translucent to transparent, and the grain shape is lathe-like with crystalline habit. It is spectrally bright and flat.

6. Results

[50] Table 2 lists the model fits. The first line is the baseline model described in section 2, a 2T-HG model using only the SHOE and an anisotropic multiple-scattering function. The next three lines show, respectively, the fits obtained using (1) a 2T-HG function and SHOE and CBOE, (2) a 3T-HG function with only the SHOE, and (3) a 3T-HG function with both SHOE and CBOE. We will primarily use the baseline model for our discussion, but include the others to illustrate the robustness of model parameters with changes in the opposition surge and phase function model. Average parameter uncertainties for our fits are included in the table footnote.

6.1. Particle Albedo (w)

[51] Not unexpectedly, the single-scattering albedo (w) was the most robust parameter characterized by the Hapke model. When values from the four model fits are compared, we find total dispersions of ~5% or less, although there are notable exceptions. The greatest dispersions were found in the dark CO-700 and CRl-450 samples. In both cases, a factor of 2 separates the extracted values when comparing 2T-HG and 3T-HG models. The two model fits are nearly indistinguishable by eye and we have included only the 2T-HG fit on the plots in Figure 5. A significant number of samples have extremely high single-scattering albedos, and our darkest samples, which are extremely dark visually, have $w \sim 0.10$.

[52] A result with significant consequences for interpretation is that the extracted single-scattering albedo differed significantly between loose and packed samples of BC and CR. If the photometric model is properly representing optical interactions among *particulates*, then the single-scattering albedo should have been the same. This finding is consistent with observations by others [*Peltoniemi and Lumme*, 1992; *Hapke*, 1999; *Shkuratov et al.*, 1999; *Näränen et al.*, 2004]. *Hapke* [1999] points out that one relevant deficiency in current analytical radiative transfer models is that they do not account for the way porosity controls factors such as the effective diffraction cross section of individual particles that are in mutual contact. As discussed later, this deficiency alone can cause retrieved values of w to be in error by as much as a factor of two.

6.2. Surface Roughness ($\bar{\theta}$)

[53] One of the more surprising results of this study is that, with few exceptions, every model inversion indicated significant surface roughness, despite efforts to make the surfaces as macroscopically smooth as possible (Table 2). The few exceptions occur when the 3T-HG is used, usually in conjunction with the CBOE model. With those exceptions this parameter is also quite robust when results from the four model fits are compared. The exceptions illustrate a problem with the Hapke model previously discussed by *Helfenstein* [1988], namely, that several parameters are correlated with the roughness parameter. In this case, we can get very different values of the roughness parameter depending upon which opposition surge model is used, even though it is generally thought that the roughness parameter is dominated by data at high phase angles [*Helfenstein and Veverka*, 1989].

[54] The roughness parameter is thought to be sensitive to scales ranging from the particle to the footprint of the detector [*Hapke*, 1984; *Helfenstein and Veverka*, 1989]. In our samples, the particulate to millimeter-scale is the only scale with any significant roughness. Since our retrieved roughness values are comparable to those published for planetary data sets, this suggests either (1) that this parameter is compensating for other photometric behavior with little physical basis or (2) that microscales dominate this parameter.

[55] To test hypothesis 1 above, we made plots of $\bar{\theta}$ versus $B0$, b, and c and found no significant correlations. However, with the exception of four files which may have aberrantly broad surge widths (CC-850, KS-550, QS, and SP), there does appear to be a weak correlation of $\bar{\theta}$ with h (Figure 6), indicating that rougher surfaces tend to have broader opposition surge widths, again suggesting a link between two properties which were thought to be dominated by opposite ends of the phase curve. A similar observation was made by *Kaasalainen* [2003].

[56] To test hypothesis 2 above, we first made a plot of $\bar{\theta}$ versus grain size (Figure 7). This plot shows no significant correlations, which is inconsistent with the findings of *Cord et al.* [2003] that a positive correlation exists. If anything, our data suggest a negative correlation. This may be because the smallest grains often form cohesive surface structures of up to a few millimeters (see Figure 3).

[57] What topographic roughness do we expect for grain scales of 10 μm–100 μm? Using a simple fractal law to model the way roughness varies with scale [cf. *Shepard and Campbell*, 1998; *Helfenstein and Shepard*, 1999], we assume that our samples were smooth to ±1 mm over the 60 mm sample dish container, giving RMS slopes of <1° at

Table 2. Best Fit Hapke Model Parameters[a]

w	h_{sh}	$B_{0,SH}$	h_{cb}	$B_{0,CB}$	$\bar{\theta}$	b or g_1	c or g_2	f	Residual
					AO 120				
0.70	**0.07**	**1.00**	**N/A**	**N/A**	**17**	**0.50**	**−0.97**	**N/A**	**0.04**
0.68	0.79	1.00	0.20	0.41	19	0.53	−1.01	N/A	0.03
0.71	0.03	0.21	N/A	N/A	17	−0.75	0.50	0.99	0.03
0.71	0.79	0.00	0.09	0.29	17	−0.67	0.49	0.99	0.03
					AO 220				
0.75	**0.04**	**0.97**	**N/A**	**N/A**	**16**	**0.37**	**−0.80**	**N/A**	**0.01**
0.75	0.00	0.00	0.16	0.25	16	0.35	−0.79	N/A	0.01
0.76	0.04	1.00	N/A	N/A	16	−0.30	0.42	0.87	0.01
0.72	0.75	0.84	0.40	0.30	17	0.04	0.52	0.77	0.01
					AO 320				
0.84	**0.02**	**0.84**	**N/A**	**N/A**	**13**	**0.30**	**−0.62**	**N/A**	**0.01**
0.80	0.12	0.43	1.44	0.37	13	0.27	−0.86	N/A	0.01
0.84	0.02	1.00	N/A	N/A	13	−0.24	0.34	0.76	0.01
0.83	0.17	1.00	0.01	0.51	10	0.00	0.63	0.57	0.01
					AO 500				
0.88	**0.02**	**0.80**	**N/A**	**N/A**	**12**	**0.29**	**−0.49**	**N/A**	**0.01**
0.87	0.00	0.00	0.17	0.20	12	0.27	−0.47	N/A	0.01
0.88	0.06	1.00	N/A	N/A	9	−0.12	0.59	0.59	0.01
0.85	0.23	0.99	0.42	0.15	0	0.77	0.00	0.36	<0.01
					BCl 450				
0.30	**0.05**	**1.00**	**N/A**	**N/A**	**20**	**0.38**	**−0.42**	**N/A**	**0.01**
0.31	0.13	0.13	0.12	0.65	20	0.34	−0.40	N/A	<0.01
0.30	0.05	1.00	N/A	N/A	19	−0.36	0.32	0.71	0.01
0.29	0.33	1.00	0.10	0.55	20	−0.25	0.48	0.72	<0.01
					BCl 550				
0.48	**0.06**	**1.00**	**N/A**	**N/A**	**20**	**0.30**	**−0.25**	**N/A**	**0.02**
0.47	0.79	0.13	0.15	0.64	20	0.28	−0.23	N/A	0.02
0.48	0.05	1.00	N/A	N/A	20	−0.30	0.31	0.62	0.02
0.44	0.52	1.00	0.14	0.51	20	−0.18	0.43	0.60	0.01
					BCl 700				
0.69	**0.04**	**0.99**	**N/A**	**N/A**	**16**	**0.28**	**−0.03**	**N/A**	**0.03**
0.58	0.02	0.71	1.49	1.00	16	0.25	−0.50	N/A	0.02
0.69	0.07	1.00	N/A	N/A	16	−0.23	0.41	0.46	0.03
0.64	0.79	1.00	0.07	0.48	18	−0.19	0.45	0.54	0.02
					BCp 450				
0.59	**0.04**	**1.00**	**N/A**	**N/A**	**13**	**0.65**	**−0.97**	**N/A**	**0.14**
0.58	0.01	0.00	0.18	1.00	14	0.61	−1.02	N/A	0.12
0.59	0.00	0.45	N/A	N/A	14	−0.80	0.64	0.99	0.13
0.53	0.02	0.00	0.15	0.72	13	0.58	0.49	1.0	0.11
					BCp 550				
0.73	**0.05**	**1.00**	**N/A**	**N/A**	**13**	**0.63**	**−0.96**	**N/A**	**0.10**
0.73	0.00	0.01	0.16	0.69	13	0.59	−1.01	N/A	0.09
0.77	0.13	0.92	N/A	N/A	13	−0.78	0.68	0.99	0.10
0.68	0.00	1.0	0.14	0.60	13	0.56	0.51	1.00	0.07
					BCp 700				
0.86	**0.05**	**1.00**	**N/A**	**N/A**	**12**	**0.61**	**−0.96**	**N/A**	**0.06**
0.85	0.08	0.72	0.13	0.44	13	0.58	−1.00	N/A	0.05
0.86	0.03	0.37	N/A	N/A	13	−0.81	0.59	0.99	0.05
0.81	0.03	1.00	0.13	0.39	12	0.55	0.72	0.00	0.04
					CC 550				
0.70	**0.06**	**1.00**	**N/A**	**N/A**	**12**	**0.35**	**−0.59**	**N/A**	**0.01**
0.71	0.04	0.01	0.08	0.51	11	0.36	−0.53	N/A	<0.01
0.71	0.06	1.00	N/A	N/A	11	−0.32	0.43	0.76	0.01
0.70	0.12	1.00	0.14	0.22	11	−0.20	0.50	0.72	<0.01
					CC 700				
0.90	**0.07**	**1.00**	**N/A**	**N/A**	**12**	**0.41**	**−0.75**	**N/A**	**<0.01**
0.90	0.09	0.90	0.01	0.93	12	0.41	−0.77	N/A	<0.01
0.90	0.07	1.00	N/A	N/A	11	−0.40	0.45	0.87	<0.01
0.89	0.33	1.00	0.04	1.00	12	−0.32	0.48	0.88	<0.01

Table 2. (continued)

w	h_{sh}	$B_{0,SH}$	h_{cb}	$B_{0,CB}$	$\bar{\theta}$	b or g_1	c or g_2	f	Residual
					CC 850				
0.95	**0.18**	**1.00**	**N/A**	**N/A**	**11**	**0.48**	**−0.88**	**N/A**	**0.01**
0.95	0.79	0.32	0.03	0.55	12	0.45	−0.84	N/A	0.01
0.95	0.15	0.95	N/A	N/A	11	−0.49	0.47	0.94	0.01
0.95	0.17	1.00	0.02	0.56	11	−0.47	0.46	0.93	<0.01
					CO 700				
0.10	**0.04**	**0.67**	**N/A**	**N/A**	**16**	**0.37**	**−0.17**	**N/A**	**<0.01**
0.10	0.08	0.00	0.12	0.48	17	0.37	−0.15	N/A	<0.01
0.21	0.08	1.00	N/A	N/A	0	−0.38	0.91	0.87	<0.01
0.19	0.11	0.55	0.78	1.00	0	−0.29	0.89	0.88	<0.01
					CRl 450				
0.23	**0.07**	**1.00**	**N/A**	**N/A**	**31**	**0.43**	**−0.18**	**N/A**	**0.02**
0.13	0.21	0.82	0.25	1.00	19	0.27	−0.57	N/A	<0.01
0.19	0.08	1.00	N/A	N/A	30	−0.44	0.23	0.55	0.01
0.12	0.25	1.00	0.27	1.00	19	−0.31	0.00	0.45	<0.01
					CRl 700				
0.53	**0.06**	**1.00**	**N/A**	**N/A**	**17**	**0.31**	**0.85**	**N/A**	**0.06**
0.43	0.43	1.00	0.19	0.87	15	0.18	1.11	N/A	0.03
0.53	0.06	1.00	N/A	N/A	17	0.34	0.00	0.23	0.05
0.48	0.19	1.00	0.11	0.58	16	−0.23	0.00	0.00	0.03
					CRp 450				
0.45	**0.05**	**0.95**	**N/A**	**N/A**	**13**	**0.37**	**−0.58**	**N/A**	**0.02**
0.44	0.01	0.00	0.19	0.65	13	0.35	−0.55	N/A	0.02
0.54	0.05	1.00	N/A	N/A	2	−0.44	0.74	0.88	0.02
0.49	0.17	1.00	0.26	0.59	0	−0.15	0.74	0.80	0.01
					CRp 700				
0.83	**0.06**	**1.00**	N/A	N/A	**13**	**0.32**	**−0.39**	N/A	**0.04**
0.83	0.45	0.00	0.14	0.72	12	0.24	−0.33	N/A	0.02
0.83	0.04	1.00	N/A	N/A	13	−0.39	0.24	0.77	0.04
0.84	0.14	1.00	0.13	0.54	0	−0.08	0.78	0.59	0.01
					FE 450				
0.10	**0.07**	**1.00**	**N/A**	**N/A**	**21**	**0.34**	**0.34**	**N/A**	**<0.01**
0.10	0.07	1.00	0.01	0.60	21	0.34	0.33	N/A	<0.01
0.11	0.07	1.00	N/A	N/A	22	−0.33	0.53	0.37	<0.01
0.10	0.51	0.99	0.26	0.67	21	−0.26	0.70	0.47	<0.01
					FE 550				
0.17	**0.07**	**1.00**	**N/A**	**N/A**	**22**	**0.34**	**0.27**	**N/A**	**<0.01**
0.13	0.40	1.00	0.16	0.54	22	0.29	0.19	N/A	<0.01
0.16	0.06	1.00	N/A	N/A	23	−0.35	−0.28	0.38	<0.01
0.15	0.37	1.00	0.28	0.74	22	−0.22	0.66	0.40	<0.01
					FE 700				
0.54	**0.06**	**1.00**	**N/A**	**N/A**	**18**	**0.29**	**0.69**	**N/A**	**0.02**
0.47	0.40	1.00	0.10	0.56	19	0.23	0.60	N/A	0.02
0.53	0.07	1.00	N/A	N/A	18	−0.29	0.21	0.18	0.02
0.48	0.34	1.00	0.10	0.55	19	−0.21	0.48	0.14	0.02
					KS 550				
0.80	**0.55**	**1.00**	**N/A**	**N/A**	**16**	**0.16**	**0.34**	**N/A**	**0.05**
0.80	0.78	0.97	0.02	0.56	17	0.18	0.23	N/A	0.04
0.80	0.55	1.00	N/A	N/A	16	−0.16	0.17	0.33	0.04
0.80	0.77	1.00	0.02	0.55	16	−0.14	0.41	0.23	0.04
					KS 850				
0.94	**0.03**	**0.51**	**N/A**	**N/A**	**6**	**0.18**	**0.85**	**N/A**	**0.03**
0.94	0.00	0.00	0.28	0.19	6	0.15	0.99	N/A	0.03
0.94	0.03	0.50	N/A	N/A	6	−0.18	0.22	0.07	0.03
0.94	0.19	0.62	0.01	0.32	0	−0.16	0.98	0.27	0.02
					MO 700				
0.13	**0.11**	**1.00**	**N/A**	**N/A**	**18**	**0.31**	**0.11**	**N/A**	**<0.01**
0.14	0.79	0.01	0.21	0.71	19	0.32	0.13	N/A	<0.01
0.14	0.09	1.00	N/A	N/A	19	−0.30	0.42	0.43	<0.01
0.15	0.09	1.00	0.01	0.45	20	−0.30	0.49	0.47	<0.01

Table 2. (continued)

w	h_{sh}	$B_{0,SH}$	h_{cb}	$B_{0,CB}$	$\bar{\theta}$	b or g_1	c or g_2	f	Residual
					OS 550				
0.95	**0.04**	**0.34**	**N/A**	**N/A**	**10**	**0.21**	**1.01**	**N/A**	**0.02**
0.94	0.01	0.03	0.62	0.20	10	0.15	1.29	N/A	0.02
0.95	0.04	0.34	N/A	N/A	19	−0.21	0.00	0.00	0.02
0.95	0.00	0.87	0.02	0.39	8	−0.25	0.95	0.10	0.01
					OS 700				
0.97	**0.01**	**1.00**	**N/A**	**N/A**	**8**	**0.19**	**0.85**	**N/A**	**0.02**
0.98	0.00	1.00	0.03	0.56	8	0.20	0.86	N/A	0.02
0.97	0.01	0.59	N/A	N/A	2	−0.23	0.03	0.28	0.01
0.97	0.01	0.59	0.00	0.56	2	−0.23	0.03	0.28	0.01
					OS 850				
0.98	**0.01**	**1.00**	**N/A**	**N/A**	**8**	**0.18**	**0.54**	**N/A**	**0.02**
0.98	0.01	0.96	0.01	0.56	8	0.18	0.54	N/A	0.02
0.98	0.01	1.00	N/A	N/A	9	−0.19	0.04	0.31	0.02
0.98	0.00	0.00	0.66	0.20	10	−0.20	0.00	0.75	0.02
					QS 550				
0.95	**0.19**	**0.36**	**N/A**	**N/A**	**12**	**0.21**	**−0.55**	**N/A**	**0.02**
0.95	0.53	0.14	0.03	0.32	12	0.23	−0.51	N/A	0.02
0.95	0.17	1.00	N/A	N/A	3	0.02	0.83	0.52	0.01
0.95	0.17	1.00	0.01	0.56	3	0.02	0.86	0.52	0.01
					SP 550				
0.996	**0.78**	**0.33**	**N/A**	**N/A**	**10**	**0.36**	**−0.80**	**N/A**	**0.01**
0.996	0.78	0.33	0.01	0.50	10	0.36	−0.80	N/A	0.01
0.996	0.10	0.73	N/A	N/A	10	−0.27	0.35	0.88	0.01
0.989	0.10	0.73	0.01	0.55	10	−0.27	0.35	0.88	0.01

[a]Each sample's top row, in bold, is for the baseline model fit with 2T-HG phase function and SHOE only. The second row keeps 2T-HG phase function but includes both SHOE and CBOE models. The third row is for a 3T-HG phase function, SHOE model only, and the fourth row is for a 3T-HG function with both SHOE and CBOE models. The last column is the residual from the fit. Using the dispersion in model parameters as a guide for our uncertainties, we estimate our average parameter uncertainties to be as follows: w (±0.02), h_{sh} (±0.21), $B_{0,SH}$ (±0.35), h_{cb} (±0.14), $B_{0,CB}$ (±0.32), $\bar{\theta}$ (±2 deg), g_1 or b (±0.09), g_2 or c (±0.18), f (±0.11).

that scale. We also assume that the surfaces are self-affine and use a Brownian scaling factor [*Shepard et al.*, 2001], giving RMS slopes of 7°–25°, a remarkable, though possibly coincidental match to the extracted model values.

[58] On the basis of their grain size, we expect samples QS, OS, and KS to be topographically and photometrically as rough as AO120, yet they have notably smaller $\bar{\theta}$. Why? As an exercise, we qualitatively compared visual estimates of roughness to model photometric roughness. We subjectively grouped our samples by their *apparent* visual roughness using the amount of pixel-to-pixel variation (inhomogeneity) in the image; this estimate of roughness took into account both the range of evident visual scales and the apparent contrast between the sample and its shadows. Our "rough" group included AO120, BCl, CO, CRl, FE, KS, and MO. Samples AO220, AO320, and AO500 were placed into an "intermediate" roughness category, and are listed in decreasing order of apparent roughness. Our "smooth" group included BCp, CC, CRp, OS, QS, and SP, the latter three primarily because there was little contrast between the sample and its shadows. We found that our subjective visual estimates of roughness corresponded, at least in broad rank order, with photometric roughness.

[59] So although QS and OS have large particle sizes and are likely among the *topographically* roughest of our samples, they are both visually and photometrically smooth. We attribute this to the lack of contrast between the sample and its shadows and hypothesize that the higher-albedo surfaces wash out shadows through multiple scattering. A plot of $\bar{\theta}$ versus single-scattering albedo supports this and shows a significant negative correlation: the brightest samples appear smoothest, and the darkest appear roughest (Figure 8). We discuss this more in section 7.

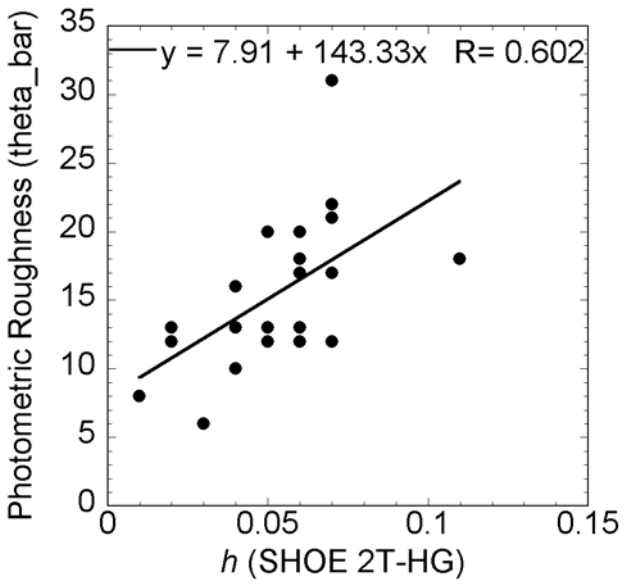

Figure 6. A plot of opposition surge width, h (SHOE only, 2T-HG function) versus $\bar{\theta}$. Uncertainties are left out for clarity.

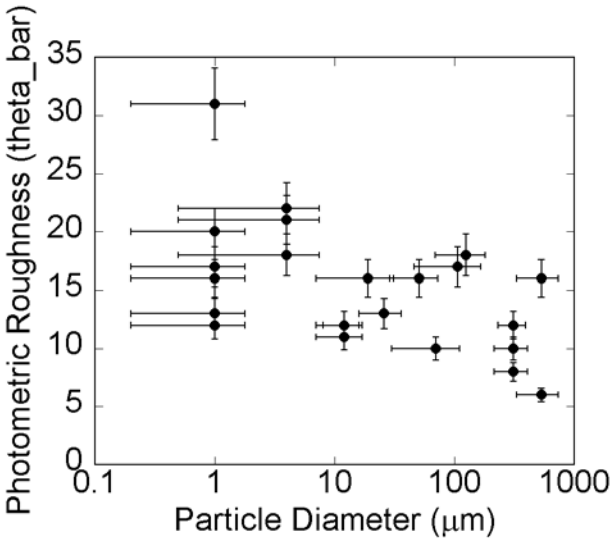

Figure 7. A plot of the photometric roughness (in degrees) versus sample grain size.

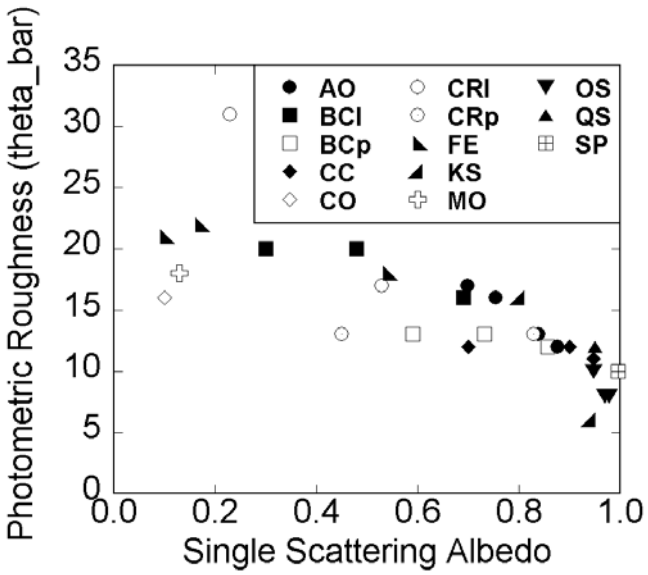

Figure 8. A plot of the photometric roughness (in degrees) versus single-scattering albedo, showing a trend suggesting bright surfaces appear photometrically smoother than dark surfaces. Uncertainties are left out for clarity.

6.3. Porosity (h)

[60] We begin this section with the caveat that although the opposition effect is evident in all of our data (see Figure 1), we only cover phase angles $\geq 3°$. Because of this limitation, we may miss features $<3°$. Our results should therefore be considered as a test of the Hapke model with moderately low phase angle coverage.

[61] As modeled by *Hapke* [1986], the width of the SHOE, h_{sh}, is given by

$$h_{sh} = -0.375 \ln(p) Y(n(r)), \quad (7)$$

where p is the porosity ($0 < p < 1$), $n(r)$ is the particle size distribution for particles of radius r, and Y is a function of the size distribution that depends upon the form of the distribution. For uniform particles, a reasonable approximation to many of our samples, $Y(n(r)) \sim 1$. Figure 9 shows a plot of h_{sh} versus $-0.375 \ln(p)$. Particles with narrow size distributions should fall along the model line. The plot suggests that either (1) the particle size distributions are not uniform or (2) the model inversion is not correct, possibly due to a lack of phase angle data $<3°$.

[62] Table 3 lists our samples, porosities, inverted h_{sh}, predicted h_{sh} given measured porosities and uniform size distributions, and the value of Y given p and h_{sh} (equation (5)). In a few cases, our values of h_{sh} and those predicted from the porosity are the same (CRl-450, FE, BCl-550). The remaining mismatches can be explained, at least partially, as a result of nonuniform particle size distributions for which there is some evidence from the images (Figures 2 and 3). For example, if the ratio of the largest to smallest diameter particle in a sample is ≤ 100, we expect Y to be 0.14–1, independent of the distribution function used; two-thirds of our samples fall within this range. However, there are still several disconcerting anomalies including AO-320, OS, CC, which are uniform within a factor of 10 based on visual inspection. Our uncertainties are large enough, however, that we cannot discount a poor fit in this region, owing to insufficient phase coverage.

[63] With few exceptions, the same samples have similar h_{sh} when measured in different wavelengths despite often having very different albedos. This suggests that most of what we are measuring is wavelength independent and likely due to SHOE alone as assumed.

[64] When looking only at the samples for which porosity is varied (BCl versus BCp and CRl versus CRp), we find no significant difference in the opposition surge width or peak. This finding is at odds with the claim that porosity is the dominant physical factor affecting the opposition surge and with the observations of *Näränen et al.* [2004].

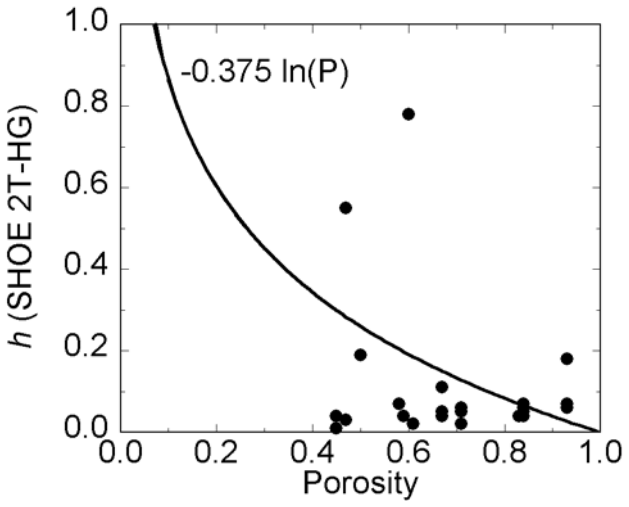

Figure 9. A plot of sample bulk porosity (fractional) versus the opposition surge width parameter, h_{sh}, showing no apparent correlations. The line is the model value for h_{sh} assuming a uniform particle size. Uncertainties are left out for clarity.

Table 3. Bulk Porosity and Opposition Surge Parameters[a]

Sample	p	w	h	h_{exp}	$Y(n(r))$
AO120	58	0.70	0.07	0.20	0.34
AO220	59	0.75	0.04	0.20	0.20
AO320	61	0.84	0.02	0.19	0.11
AO500	71	0.88	0.02	0.13	0.16
BCl-450	84	0.29	0.05	0.07	0.76
BCl-550	84	0.47	0.06	0.07	0.92
BCl-700	84	0.64	0.04	0.07	0.61
BCp-450	67	0.58	0.04	0.15	0.27
BCp-550	67	0.73	0.05	0.15	0.33
BCp-700	67	0.86	0.05	0.15	0.33
CC-550	93	0.71	0.06	0.03	2.20
CC-700	93	0.90	0.07	0.03	2.57
CC-850	93	0.95	0.18	0.03	6.61
CO-700	83	0.10	0.04	0.07	0.57
CRl-450	84	0.24	0.07	0.07	1.07
CRl-700	84	0.62	0.06	0.07	0.92
CRp-450	71	0.51	0.05	0.13	0.39
CRp-700	71	0.86	0.06	0.13	0.47
FE-450	84	0.09	0.07	0.07	1.07
FE-550	84	0.15	0.07	0.07	1.07
FE-700	84	0.53	0.06	0.07	0.92
KS-550	47	0.80	0.55	0.28	1.94
KS-850	47	0.94	0.03	0.28	0.11
MO-700	67	0.13	0.11	0.15	0.73
OS-550	45	0.95	0.04	0.30	0.13
OS-700	45	0.98	0.01	0.30	0.03
OS-850	45	0.98	0.01	0.30	0.03
QS-550	50	0.94	0.19	0.26	0.73
SP-550	60	1.00	0.79	0.19	4.07

[a]Value p is bulk porosity (in percent), w is the single-scattering albedo, h is the inverted opposition surge width using a 2T-HG with SHOE only, h_{exp} is the expected value of h given the porosity and assuming a uniform particle size distribution (equation (7)), and $Y(n(r))$ is the ratio of our inverted to expected h.

[65] We found it difficult to obtain unique fits when modeling with both SHOE and CBOE. Others have suggested that the only way to separate the two is to use polarized data [cf. *Hapke et al.*, 1998; *Nelson et al.*, 2000; *Shkuratov et al.*, 2002; *Hapke*, 2002] which are unavailable in the BUG lab and most spacecraft cameras and radiometers. Without polarization data to constrain them, the CBOE and SHOE models appear to play off of one another to minimize χ^2 with little physical basis. An exception to this may be when phase angle coverage to near 0° is available [cf. *Helfenstein et al.*, 1997].

6.4. Transparency ($B_{0,SH}$)

[66] Most samples had best fit values of $B_{0,SH} = 1$ (its limiting value), indicating (see section 2.3) that their scatterers are opaque. The brightest surfaces tended to have $B_{0,SH} < 1$, consistent with the interpretation that they are more transparent (like QS or SP) or are composed of transparent materials, but have relatively high densities of deep internal scatterers. In the case of several OS and KS fits, the samples are so bright that we suspect a type of "retroreflection" to be involved. First proposed by *Oetking* [1966] and *Trowbridge* [1978], retroreflection occurs when grain regularities give rise to Fresnel reflections in the backscatter direction (see the specular glints in Figure 2). This is not accounted for in the *Hapke* [1986] model.

6.5. Grain Structure (Phase Function)

[67] Although we inverted the data using both 2T-HG and 3T-HG phase functions, in this section, we limit our discussion to the results obtained with the 2T-HG model with only SHOE.

[68] As noted earlier, the form of the particle phase function is strictly empirical; however, qualitative physical characteristics have been attributed to values of b and c. *McGuire and Hapke* [1995] measured the phase function of numerous large particles and generalized their behavior. Here we look at their major conclusions and compare them to our results (Figure 10).

[69] According to *McGuire and Hapke* [1995], particles with large numbers of internal scatterers have low values of b and positive c (backscattering). Decreasing the absorption of these particles increases both w and c, but does not affect b. For the samples that fall in this category (CR, FE, KS, OS), this trend holds with the exception of OS. However, this sample is extremely bright at all three wavelengths at which it was measured and its validity as a test case may be questioned.

[70] *McGuire and Hapke* [1995] found that particles with few internal scatterers had high values of b and negative c (forward scatterers). Spherical transparent particles have the highest amount of forward scattering and narrowest lobes; as these particles become more absorbing (i.e., as w decreases), b decreases slightly (lobe width decreases), and c does not change. Our most transparent particles, at least visually, were QS and SP. Both plot in moderate to low internal scattering region of the reversed J, although not in the toe of the "J" where ideally transparent particles are expected to plot. Because the shadow-hiding opposition effect $B_{0,SH}$ parameter also provides a measure of transparency (see section 6.4.), one might expect that samples with the smallest values of $B_{0,SH}$ would also exhibit either relatively large negative values of the c parameter (i.e., be forward-scattering) or else have large positive values of c (i.e., be backward-scattering by virtue of a high density of internal scatterers embedded in a transparent matrix). This is, in fact, the case. SP and QS have the smallest values of $B_{0,SH}$ (0.33 and 0.36, respectively), and they also have relatively large negative values of c (-0.80 and -0.55, respectively). The OS (at 550 nm wavelength) and KS samples also have relatively small values of $B_{0,SH}$ (0.34 and 0.51, respectively), and they also have high positive values of c (1.01 and 0.85, respectively). The latter are appropriate because the OS grains have a "pearly" appearance and the KS sand is largely made up of similarly translucent particles, probably caused by a high density of internal scatterers.

[71] Sample CC fits the *McGuire and Hapke* [1995] expectations: as w increases, b increases and c changes only slightly so that samples become more forward scattering with increasing albedo. This sample's particles are spheroidal, and may also be relatively transparent although their small size makes that difficult to verify.

[72] Samples BCp and AO do not match expectations; both see an increase in lobe width (b) with a decrease in albedo. However, some of this effect for AO may be related to a corresponding change in particle size. Nevertheless, neither sample can be characterized as clear or having a low density of internal scatterers. We believe Fresnel reflections from grain surfaces are responsible for the observed behavior; in the AO sample the reflections are probably due to the regular habit of the particles, while the BCp surface has been compressed, possibly aligning the clay particles in a

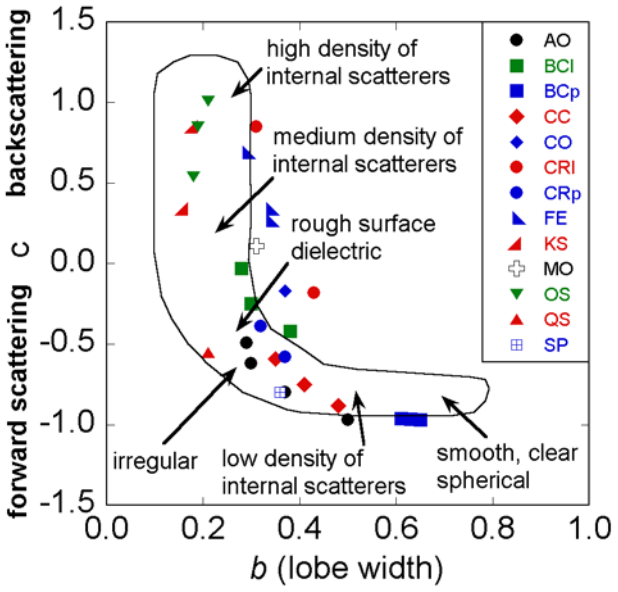

Figure 10. A plot of our best fit two-term Henyey-Greenstein phase function parameters, superimposed upon the reverse "J" field discussed by *McGuire and Hapke* [1995]. Uncertainties are left out for clarity.

horizontal layer. While not showing a direct specular peak, these samples nevertheless had strong forward scattering behavior that may have been a type of specular "gloss" [*Kortum*, 1969; *Shepard et al.*, 1993]. The Hapke model does not explicitly include Fresnel reflection from the surface.

[73] The packing state of our samples appears to affect the inversions of particle phase function. The loose and packed BC and CR samples had significantly different particle phase functions. As with the single-scattering albedo, if this property is strictly related to the particles it should be unaffected by packing state.

7. Discussion

[74] What optical and mechanical properties can we confidently extract from photometric data obtained between phase angles of 3° to 130°?

7.1. Single-Scattering Albedo

[75] The single-scattering albedo is probably the most robust parameter that can be extracted: it appears to be the least affected by the choice of other model parameters. In general, particle size is thought to be but one parameter affecting the single-scattering albedos of individual particles. Examination of the AO photometric behavior, in which particle size was the major difference, supports the notion that, everything else being equal, the smaller particles are the brightest. However, an examination of the rest of our samples makes it clear that retrieved values of single-scattering albedo are being influenced by porosity and roughness-dependent factors that are not given adequate account in the Hapke model. In particular, two samples (BC and CR) gave significantly different single-scattering albedos in different packing states. On the basis of these samples, decreasing the bulk porosity and/or surface roughness increases retrieved values of w. We cannot determine the extent to which each of these factors is more important, but both trends have been observed or predicted by others [*Hapke*, 1999; *Kaasalainen*, 2003; *Näränen et al.*, 2004].

[76] *Hapke* [1999] notes that one difficulty with radiative transfer models is that the media is assumed to be continuous and porosity is not a factor in the reflectance (other than the opposition surge – a separate component). However, discrete media models, such as that of *Shkuratov et al.* [1999], do account for interparticle spacing. A comparison of simple radiative transfer and discrete models shows that the radiative transfer model underestimates – by factors as high as two – the reflectance of a packed medium [*Hapke*, 1999]. This appears to be the case with our samples. We find that the extracted value of w is not simply the single-scattering albedo of individual particles, but a composite parameter that includes particle single-scattering albedo, regolith packing state, and possibly surface roughness. This is more consistent with the interpretation of w as the volume single-scattering albedo [see *Hapke*, 1993, p. 172] and at odds with the more common interpretation that it is a property of individual particles. Future laboratory work to explore this relationship may be fruitful, especially with comminuted grains where small grains can efficiently pack interstices.

7.2. Photometric Roughness

[77] Our samples had $\overline{\theta}$ between 6° and 31°, similar to values extracted from solar system objects, despite having no macroscopic roughness at scales greater than a few millimeters. We conclude that surface roughness at scales ranging from the particle to a few millimeters is sufficient to explain photometric roughness on most planetary objects. Larger scales of roughness may make an additional minor contribution.

[78] Photometric roughness appears to decrease with increasing albedo, so that any retrieved value should be considered a lower limit. In bright samples of large particulate size where we expect large microtopography (OS, QS, KS), the samples are visually and photometrically smooth. The KS sample is telling; at 550 nm, $w = 0.80$ and $\overline{\theta} = 16°$, while at 850 nm, $w = 0.94$ and $\overline{\theta} = 6°$. These results are consistent with past and recent work. *Hapke* [1984, 1993] noted that his roughness model would be strictly true only for dark surfaces and that increased albedo would negate shadowing and photometrically smooth the surface. This is evident in the OS, QS, and SP samples; all appear visually smooth because there is little contrast between grains and interstices where shadows should appear. *Buratti and Veverka* [1985] first confirmed an albedo effect in a simple experimental test and discussed how this might affect interpretations of the brighter icy satellites. Using numerical simulations of fractal surfaces as a guide, *Shepard and Campbell* [1998] suggested that (1) the smallest and roughest scales dominate the photometric roughness of a surface and (2) the smallest scales are defined as those at which multiple scattering erases shadows. Since surfaces with higher w have greater multiple scattering, the scales at which shadows are erased on such surfaces will be larger than for dark surfaces. On fractal surfaces, the best analog

for planetary terrain [cf. *Shkuratov and Helfenstein*, 2001; *Shepard et al.*, 2001], larger scales are smoother; therefore brighter surfaces should appear smoother than dark surfaces. More recent modeling work by *Shkuratov et al.* [2005] is also consistent with this interpretation.

[79] From the point of view of an interpreter of photometric roughness, this finding may require "recalibration" of what photometric roughness is actually referring to. Under one possible scenario, astronauts could walk on two different surfaces as flat as a terrestrial parking lot, noting little difference in what is typically perceived as roughness, and yet each surface may exhibit very different photometric roughness depending upon its microscale structure and albedo.

7.3. Opposition Surge

[80] The opposition surge is often touted as the best way to get at the state of surface compaction or bulk porosity. With our admittedly imperfect data, we find little correspondence between relative or absolute values of bulk porosity and our extracted opposition surge parameters. The expected dependence of both porosity and the size distribution function on the SHOE surge width makes this a difficult problem in the best cases but we have attempted to minimize this complication by using relatively uniform samples. Surge widths tended to be consistent even with variations in wavelength (and hence albedo), suggesting little influence by the CBOE. Including the CBOE in the model inversions was of little help and, given the additional parameters to fit, allowed the model inversions to range widely with little constraint. We observed a weak correlation between $\overline{\theta}$ and h_{sh}, suggesting that these two parameters are sensitive to the same scales and may compensate for each other.

[81] Because recent experimental work by *Hapke et al.* [1998], *Nelson et al.* [2000], and others suggests that observations in circularly polarized light are required to separate the effects of the two mechanisms, it may not be possible to make any meaningful inferences about planetary surface porosity from unpolarized observations; this includes nearly all spacecraft and telescopic observations, and many laboratory studies including our own. This conclusion must be considered our most tentative, however, since our data are limited to phase angles $\geq 3^\circ$ and our model parameter uncertainties are significant. Since most solar system objects are primarily observed at low phase angles, discovering what, if any, physical attributes can be uniquely determined from the opposition surge should be a priority for future laboratory work in photometry.

7.4. Phase Function

[82] The phase function of a surface appears to give a gross sense of the type of particulate involved in scattering and our observations generally fall within the parameter space outlined by *McGuire and Hapke* [1995]. However, we find a number of exceptions to their rules. Additionally, the phase function appears to be affected by the sample packing state—another sign that the photometric model does not adequately treat optical interactions that are controlled by factors like porosity and roughness. Here, as with the single-scattering albedo, the continuous medium assumption of radiative transfer models may be the cause. We conclude that the retrieved phase function parameters are, as with single-scattering albedo, not necessarily diagnostic of the individual particles making up the surface.

7.5. Synthesis

[83] Our own results and recent work by others point to deficiencies in the Hapke model that future developments need to address. A well-known deficiency in the Hapke model is that it treats only whole particles as the fundamental light-scattering units. There is increasing evidence that, at least at some phase angles, smaller scatterers such as particle internal defects, inclusions, and grain-surface asperities play an important role as fundamental light scatterers [*Shkuratov et al.*, 1999; *Hapke*, 1999; *Hillier and Buratti*, 2001; *Piatek et al.*, 2004]. Indeed, the coherent backscattering effect almost certainly occurs within individual particles as well as between adjacent particles [cf. *Hillier*, 1997; *Hillier and Buratti*, 2001; *Shepard and Arvidson*, 1999; *Hapke*, 2002].

[84] Given the proposed importance of subparticle-scale scatterers, it was surprising to find that some of the most critical errors in our retrieved Hapke parameters arise from optical interactions among *whole particles* that are not adequately modeled. This was demonstrated in our study by the fact that retrieved values of single-scattering albedo and particle phase function parameters, supposedly intrinsic particle properties, could be significantly altered by changing the packing state. From this result and *Hapke* [1999], it is clear that the effects of porosity need to be incorporated in his bidirectional reflectance equation.

[85] Our results indicate that "macroscopic" roughness and the shadow-hiding opposition effect occur on overlapping size scales; that is, over size scales comparable to individual soil grains and clumps of grains. This suggests that the two components may better be modeled as a single phenomenon rather than as separate, distinct contributions. It is also clear that, especially for applications to highly reflective surfaces like icy satellites in the outer solar system, Hapke's macroscopic roughness correction needs to account for multiple scattering of light between topographic facets of surface relief.

8. Conclusions

[86] The prospect for extracting unique and meaningful physical information about a planetary surface, especially its particulate properties, from the Hapke model in its present form needs to be reevaluated. Clearly, the observed photometric behavior of soils or regolith is a composite effect of optical interactions at many scales and by numerous mechanisms – it cannot readily be inverted into the properties of individual particles [*Shkuratov and Helfenstein*, 2001]. From this work, we conclude that, at its current stage of development, the Hapke model does not adequately treat optical interactions in particulate samples with sufficient fidelity to be utilized as a reliable remote sensing tool for estimating unique and meaningful physical properties of planetary surfaces. Retrieved values of the Hapke model parameters generally do not accurately represent the properties of the particulates alone, but rather some complex combination of particulate properties, surface roughness, and packing state.

[87] **Acknowledgments.** We thank B. Hapke, Y. Shkuratov, and an anonymous reviewer for their insights and comments, which greatly improved the manuscript. The authors are grateful to many who provided assistance or materials for this work including B. Graboski, B. Wilcox, C. Hallen, L. Tanner, C. Venn, G. Chamuris, and S. Baker. This research was supported by NASA PGG NAG5-11539 to M.K.S. and NAG5-11492 to P.H.

References

Akimov, L. A. (1988), Light reflection from the Moon: 1, *Kinematica Fiz. Nebesnykh Tel.*, *4*, 3–10.

Buratti, B., and J. Veverka (1985), Photometry of rough planetary surfaces: The role of multiple scattering, *Icarus*, *64*, 320–328.

Buratti, B., M. D. Hicks, L. A. Soderblom, D. Britt, J. Oberst, and J. Hillier (2004), Deep Space 1 photometry of the nucleus of Comet 19P/Borrelly, *Icarus*, *167*, 16–29.

Chandrasekhar, S. (1960), *Radiative Transfer*, Dover, Mineola, N. Y.

Cord, A. M., P. C. Pinet, Y. Daydou, and S. Chevrel (2003), Experimental determination of the Hapke shadowing function parameter for planetary regolith surface analogs, *Lunar Planet. Sci.*, *XXXIV*, abstract 1349.

Cruikshank, D. P., C. M. Dalle Ore, T. L. Roush, T. R. Geballe, T. C. Owen, C. de Bergh, M. D. Cash, and W. K. Hartmann (2001), Constraints on the composition of Trojan asteroid 624 Hector, *Icarus*, *153*, 348–360.

Hapke, B. (1981), Bidirectional reflectance spectroscopy: 1. Theory, *J. Geophys. Res.*, *86*, 3039–3054.

Hapke, B. (1984), Bidirectional reflectance spectroscopy, 3: Correction for macroscopic roughness, *Icarus*, *59*, 41–59.

Hapke, B. (1986), Bidirectional reflectance spectroscopy, 4: The extinction coefficient and opposition effect, *Icarus*, *67*, 264–280.

Hapke, B. (1993), *Theory of Reflectance and Emittance Spectroscopy*, Cambridge Univ. Press, New York.

Hapke, B. (1999), Scattering and diffraction of light by particles in planetary regoliths, *J. Quant. Spectrosc. Radiat. Transfer*, *61*, 565–581.

Hapke, B. (2002), Bidirectional reflectance spectroscopy, 5: The coherent backscatter opposition effect and anisotropic scattering, *Icarus*, *157*, 523–534.

Hapke, B., and E. Wells (1981), Bidirectional reflectance spectroscopy: 2. Experiments and observations, *J. Geophys. Res.*, *86*, 3055–3060.

Hapke, B. W., R. M. Nelson, and W. D. Smythe (1998), The opposition effect of the Moon: Coherent backscattering and shadow hiding, *Icarus*, *133*, 89–97.

Hartman, B., and D. Domingue (1998), Scattering of light by individual particles and the implications for models of planetary surfaces, *Icarus*, *131*, 421–448.

Helfenstein, P. (1985), Derivation and analysis of geological constraints on the emplacement and evolution of terrains on Ganymede from applied differential photometry, Ph.D. thesis, 426 pp., Brown University, Providence, R. I.

Helfenstein, P. (1988), The geological interpretation of surface roughness, *Icarus*, *73*, 462–481.

Helfenstein, P., and M. K. Shepard (1999), Submillimeter-scale topography of the lunar regolith, *Icarus*, *141*, 107–131.

Helfenstein, P., and J. Veverka (1989), Physical characterization of asteroid surfaces from photometric analysis, in *Asteroids II*, edited by R. Binzel, T. Gehrels, and M. S. Matthews, pp. 557–593, Univ. of Ariz. Press, Tucson.

Helfenstein, P., J. Veverka, and J. Hillier (1997), The lunar opposition effect: A test of alternative models, *Icarus*, *128*, 2–14.

Hillier, J. K. (1997), Scattering of light by composite particles in a planetary surface, *Icarus*, *130*, 328–335.

Hillier, J. K., and B. Buratti (2001), Monte Carlo simulations of light scattering by composite particles in a planetary surface, *Icarus*, *149*, 251–261.

Hudson, R. S., and S. J. Ostro (1999), Physical model of asteroid 1620 Geographos from radar and optical data, *Icarus*, *140*, 369–378.

Kaasalainen, S. (2003), Laboratory photometry of planetary regolith analogs. I, Effects of grain density and packing properties on opposition effect, *Astron. Astrophys.*, *409*, 765–769.

Kortum, G. (1969), *Reflectance Spectroscopy*, Springer, New York.

Lumme, K., and E. Bowell (1981), Radiative transfer in the surfaces of atmosphereless bodies. I. Theory, *Astron. J.*, *86*, 1694–1704.

Mallama, A., D. Wang, and R. A. Howard (2002), Photometry of Mercury from SOHO/LASCO and Earth: The phase function from 2 to 170°, *Icarus*, *155*, 253–264.

McGuire, A. F., and B. W. Hapke (1995), An experimental study of light scattering by large, irregular particles, *Icarus*, *113*, 134–155.

Mishchenko, M. I. (1992), Polarization characteristics of the coherent backscatter opposition effect, *Earth Moon Planets*, *58*, 127–144.

Muinonen, K. (1990), Light scattering by inhomogeneous media: Backward enhancement and reversal of linear polarization, Ph.D. thesis, Univ. of Helsinki, Helsinki, Finland.

Näränen, J., S. Kaasalainen, J. Peltoniemi, S. Heikkilä, M. Granvik, and V. Saarinen (2004), Laboratory photometry of planetary regolith analogs. II, Surface roughness and extremes of packing density, *Astron. Astrophys.*, *426*, 1103–1109.

Nelson, R. M., B. W. Hapke, W. D. Smythe, and L. J. Spilker (2000), The opposition effect in simulated planetary regoliths: Reflectance and circular polarization ratio change at small phase angles, *Icarus*, *147*, 545–558.

Oetking, P. (1966), Photometric studies of diffusely reflecting surfaces with applications to the brightness of the Moon, *J. Geophys. Res.*, *71*, 2513–2525.

Peltoniemi, J., and K. Lumme (1992), Light scattering by closely packed particulate media, *J. Opt. Soc. Am. A Opt. Image Sci.*, *9*, 1320–1326.

Piatek, J. L., B. W. Hapke, R. M. Nelson, W. D. Smythe, and A. S. Hale (2004), Scattering properties of planetary regolith analogs, *Icarus*, *171*, 531–545.

Poulet, F., J. N. Cuzzi, D. P. Cruikshank, T. Roush, and C. M. Dalle Ore (2002), Comparison between the Shkuratov and Hapke theories for solid planetary surfaces: Applications to the surface composition of two Centaurs, *Icarus*, *160*, 313–324.

Seeliger, H. (1895), Theorie der beliuchtung staubformiger Kosmischen masses insbesondre des Saturnringes, *Abhandl. Bayer akad. Wiss. Math. Nature, K1, II*, *18*, 1–72.

Shepard, M. K., and R. E. Arvidson (1999), The opposition surge and photopolarimetry of fresh and coated basalts, *Icarus*, *141*, 172–178.

Shepard, M. K., and B. A. Campbell (1998), Shadows on a planetary surface and implications for photometric roughness, *Icarus*, *134*, 279–291.

Shepard, M., R. E. Arvidson, and E. A. Guinness (1993), Specular scattering on a terrestrial playa and implications for planetary surfaces, *J. Geophys. Res.*, *98*, 18,707–18,718.

Shepard, M. K., B. A. Campbell, M. H. Bulmer, T. G. Farr, L. R. Gaddis, and J. J. Plaut (2001), The roughness of natural terrain: A planetary and remote sensing perspective, *J. Geophys. Res.*, *106*, 32,777–32,795.

Shkuratov, Y. G., and P. Helfenstein (2001), The opposition effect and the quasi-fractal structure of regolith: I. Theory, *Icarus*, *152*, 96–116.

Shkuratov, Y. G., and D. G. Stankevich (1997), Brightness distribution over the lunar disk at zero phase angle, *Sol. Syst. Res.*, *31*, 213–218.

Shkuratov, Y. G., K. Muinonen, E. Bowell, K. Lumme, J. I. Peltoniemi, M. A. Kreslavsky, D. G. Stankevich, V. P. Tishkovetz, N. V. Opanasenko, and L. Y. Melkumova (1994), A critical review of theoretical models of negatively reflected polarized light scattered by atmosphereless solar system bodies, *Earth Moon Planets*, *65*, 201–246.

Shkuratov, Y. G., D. G. Stankevich, A. A. Ovcharenko, and V. V. Korokhin (1997), A study of light backscattering from planetary-regolith-type surfaces at phase angles 0.2°–3.5°, *Sol. Syst. Res.*, *31*, 50–56.

Shkuratov, Y., L. Starukhina, H. Hoffmann, and G. Arnold (1999), A model of spectral albedo of particulate surfaces: Implication to optical properties of the Moon, *Icarus*, *137*, 235–246.

Shkuratov, Y. G., A. Ovcharenko, E. Zubko, O. Miloslavskaya, K. Muinonen, J. Piironen, R. Nelson, W. Smythe, V. Rosenbush, and P. Helfenstein (2002), The opposition effect and negative polarization of structural analogs for planetary regoliths, *Icarus*, *159*, 396–416.

Shkuratov, Y. G., D. G. Stankevich, D. V. Petrov, P. C. Pinet, A. M. Cord, Y. H. Daydou, and S. D. Chevrel (2005), Interpreting photometry of regolith-like surfaces with different topographies: Shadowing and multiple scattering, *Icarus*, *173*, 3–15.

Simonelli, D. P., J. Veverka, P. C. Thomas, P. Helfenstein, and B. Carcich (1996), Ida lightcurves: Consistency with Galileo shape and photometric models, *Icarus*, *120*, 38–47.

Trowbridge, T. (1978), Retroreflection from rough surfaces, *J. Opt. Soc. Am.*, *68*, 1225–1242.

P. Helfenstein, Center for Radiophysics and Space Research, Cornell University, 320 Space Sciences Bldg., Ithaca, NY 14853-6801, USA.

M. K. Shepard, Department of Geography and Geosciences, Bloomsburg University, 400 E. Second St., Bloomsburg, PA 17815, USA. (mshepard@bloomu.edu)